Comput Mech (2014) 54:943–953
DOI 10.1007/s00466-014-0976-6

ORIGINAL PAPER

Patient-specific analysis of post-operative aortic hemodynamics: a focus on thoracic endovascular repair (TEVAR)

F. Auricchio · M. Conti · A. Lefieux · S. Morganti · A. Reali · F. Sardanelli · F. Secchi · S. Trimarchi · A. Veneziani

Received: 12 November 2013 / Accepted: 6 January 2014 / Published online: 24 January 2014
© Springer-Verlag Berlin Heidelberg 2014

Abstract The purpose of this study is to quantitatively evaluate the impact of endovascular repair on aortic hemodynamics. The study addresses the assessment of post-operative hemodynamic conditions of a real clinical case through patient-specific analysis, combining accurate medical image analysis and advanced computational fluid-dynamics (CFD). Although the main clinical concern was firstly directed to the endoluminal protrusion of the prosthesis, the CFD simulations have demonstrated that there are two other important areas where the local hemodynamics is impaired and a disturbed blood flow is present: the first one is the ostium of the subclavian artery, which is partially closed by the graft; the second one is the stenosis of the distal thoracic aorta. Besides the clinical relevance of these specific findings, this study highlights how CFD analyses allow to observe important flow effects resulting from the specific features of patient vessel geometries. Consequently, our results demonstrate the potential impact of computational biomechanics not only on the basic knowledge of physiopathology, but also on the clinical practice, thanks to a quantitative extraction of knowledge made possible by merging medical data and mathematical models.

Keywords Computational fluid dynamics (CFD) · Biomechanics · Aorta · Endograft · Patient-specific

1 Introduction

Thoracic endovascular aortic repair (TEVAR) is a minimally invasive approach for the treatment of thoracic aortic disease, such as dissections[1] or aneurysms[2]; the treatment consists of the deployment of one or more stent-grafts, i.e., metallic tubular wireframe covered by a Dacron skirt, to divert the blood flow.

Although its long-term results are still controversial [6], TEVAR has been rapidly adopted into clinical practice. Similar to other endovascular approaches, the outcomes of TEVAR rely on an appropriate balance between the biomechanical features of the prosthesis and those of the target vascular anatomy. This is difficult to achieve, as demonstrated by the frequency and variety of device-related complications (device compression, invagination, misaligned deployment, and kinks or aortic perforation). Obviously, anatomical complexity continues to be the most important reason for early and late stent-graft failure. In particular, one of the extremities of the device lands at the level of the aortic arch; due to the stiffness of the stent-graft, very angulated arches may cause a reduction in the area of contact with the aortic wall. Specifically, the lack of apposition of the device to the aor-

F. Auricchio · M. Conti (✉) · S. Morganti · A. Reali
University of Pavia, Pavia, Italy
e-mail: michele.conti@unipv.it

F. Auricchio · A. Lefieux
Institute for Advanced Study (IUSS), Pavia, Italy

F. Sardanelli · F. Secchi · S. Trimarchi
IRCCS Policlinico San Donato, Milan, Italy

F. Sardanelli
Dipartimento di Scienze Biomediche per la Salute,
Universit degli Studi di Milano, Milan, Italy

A. Veneziani
Department of Mathematics and Computer Science,
Emory University, Atlanta, GA, USA

[1] Delamination of the vessel wall layers creating a *false* lumen, which results in an undesired alternative path for the bloodstream, normally flowing through the native *true* lumen.

[2] Abnormal, local enlargement of the vessel diameter.

tic wall along the inner curvature of the aortic arch results in the so-called *bird-beak* configuration, which is the radiologic detection of a wedge-shaped gap between the undersurface of the stent graft and the aortic wall [24].

The clinical literature discussing the incidence of bird-beak effect and its impact on procedure outcomes is very heterogeneous and somehow contradictory [3,12,13,21]. In particular, the retrospective study of Ueda and colleagues [24] suggests that the presence of bird-beak configuration after TEVAR for a pathologic aortic arch condition is significantly correlated with the risk of endoleak[3] occurring at the proximal landing zone[4] or from left subclavian artery. Furthermore, the longer the bird-beak length, the higher the risk for endoleak formation. These conclusions have been recently reconsidered by Kasirajan et al. [13] who, however, underline that bird-beak is not desirable because of the loss of sealing zone within the aortic neck and of the abluminal graft surface exposure to the force of the bloodstream.

All these clinical concerns call for a quantitative analysis of post-operative aortic hemodynamics and its correlation with outcomes. In this study, we investigate a real clinical case presenting a bird-beak configuration after TEVAR. We perform computational fluid dynamics (CFD) analysis on the patient-specific vascular models derived from medical images. We discuss the results and establish some comparisons with similar cases investigated in the literature. We also present a preliminary comparison of the numerical results with the real blood flow measured by magnetic resonance.

2 Material and methods

In the following we illustrated the adopted workflow, highlighting, in particular, how we generate the computational domains from medical images regarding the specific clinical case under investigation.

2.1 Clinical summary and medical imaging

The patient is a 51-year-old male suffering hypertension and having an asymptomatic post-dissecting thoracic aortic aneurysm with a maximum diameter of 6.1 cm. Given his condition, the patient was selected for endovascular exclusion of the aneurysm using two cTAG stent-grafts (conformable TAG, W.L. GORE & Associates. Inc., Flagstaff, Arizona, USA), sized 34–34–20 and 28–28–15 mm, with the proximal landing zone covering the origin of the left subclavian artery. At 6 month follow-up, imaging showed successful exclusion of the aneurysm without endoleak but the post-operative multislice computed tomography (MSCT) scan showed a bird-beak configuration of the proximal prosthesis as depicted in Fig. 1. Further collection of clinical data and medical images has been performed also one year after the intervention. In particular, magnetic resonance imaging (MRI) was performed using a 1.5-T unit with 40-mT/m gradient power (Magnetom Sonata Maestro Class, Siemens, Erlangen, Germany) and a four-channel cardio-thoracic coil. Electrocardiographically-triggered free-breathing through-plane and in-plane phase-contrast (PC) sequences was performed for phase-velocity mapping of aortic and branches flow with following technical parameters: TR/TE = 4/3.2 ms, thickness 5 mm, velocity encoding from 150 to 350 ms, and temporal resolution 41 ms.

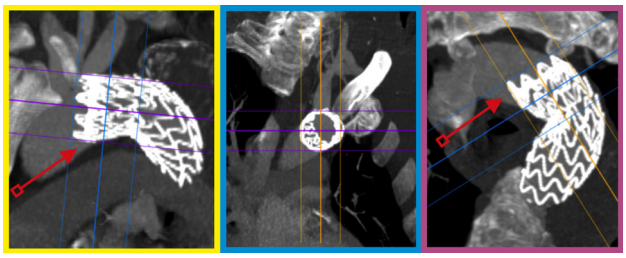

Fig. 1 Multislice computed tomography with intravenous contrast agent administration. Thin-slab maximum intensity projection shows bird-beak configuration. At proximal end, the stent-graft has an imperfect apposition to the lesser inner curve of aortic arch, resulting in a wedge-shaped gap (see *red arrow*) between undersurface of the stent-graft and aortic wall

2.2 Image processing: segmentation and reconstruction of aortic lumen profile

One of the key steps of our study is the analysis of vascular anatomy before and after the implant. For this reason we have performed an accurate image processing of two MSCT datasets: (i) pre-operative scan performed few days before the surgery; (ii) post-operative scan performed few days after the surgery. The goal of this step is twofold, consisting of: (i) evaluation of the anatomical changes induced by the procedure; (ii) generation of the computational grid to be used in the CFD analyses.

MSCT was performed using a 16-slice unit (150 mAs, 110 kVp; acquisition thickness 5 mm, pitch 1.5; reconstruction thickness 1.2 mm), before and after intravenous administration of 100 mL of iodinated contrast material; the contrast-enanched scan started after the arrive of the contrast in aortic arch.

The comparison between pre- and post-operative graft-vessel configuration relies on a precise assessment and recon-

[3] An endoleak is a persistent blood flow within the aneurysm sac after endovascular aortic repair; different types of endoleaks (I–IV) are described.

[4] Vascular region corresponding to one of the stent-graft extremities, where the adhesion between the prosthesis and the vessel wall is essential to guarantee the implant stability.

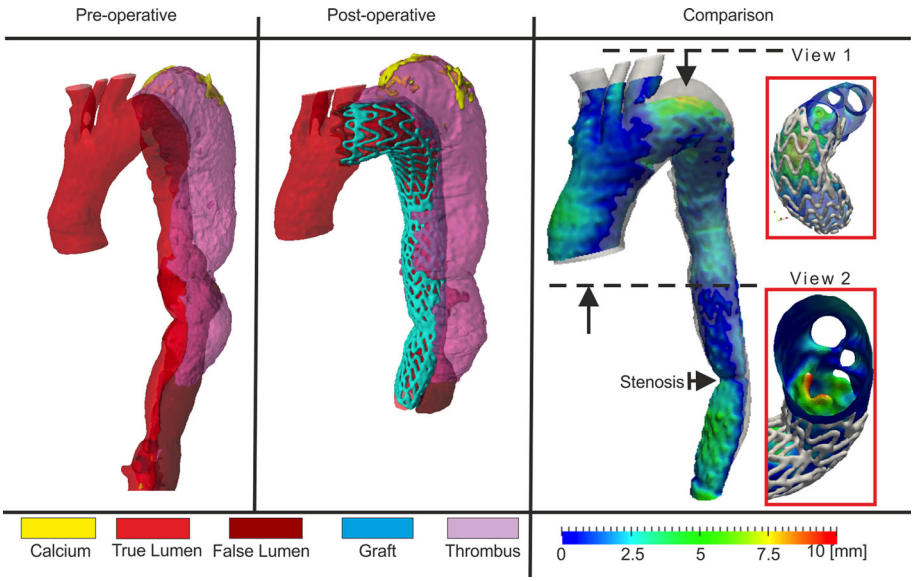

Fig. 2 3D reconstruction of pre-operative (*left panel*) and post-operative aorta (*middle panel*). The comparison between the two configurations is shown in the *right panel* where the point-wise distance between the post- and pre-operative configuration is depicted

struction of the 3D profile of vessel lumen, thrombus, and calcifications. Obviously, the segmentation of the post-operative case should include also the stent-grafts. For this reason, according to the approach proposed in [2], we perform the image segmentation of the two MSCT datasets using the open-source software ITK-Snap [25] obtaining the 3D reconstructions depicted in Fig. 2.

The resulting 3D model can be exported in stereolithography representation (STL format), which can be subsequently elaborated for the purpose of CFD simulation. Given the goal of the study, the 3D reconstructions of thrombus, calcifications and stent-grafts have been included in the model just for visualization. In fact, we are mainly interested in the surface defining pre- and post-operative aortic lumen in order to define the volume domain for CFD analysis as described in Sect. 2.4.

Using the pre- and post-operative 3D lumen profiles, we have performed a preliminary analysis to evaluate the change induced by the graft apposition. First, we have registered the post-operative lumen profile onto the pre-operative one using the module *vmtkicpregistration*, available within the library Vascular Modeling Toolkit (VMTK-http://www.vmtk.org). In a second step, we have measured the point-wise distance between the two surfaces using the VMTK module *vmtksurfacedistance*.

The results of such a preliminary analysis, depicted in Fig. 2, show that the proximal graft protrudes into the lumen at the level of the inner curvature of the arch (i.e., a bird-beak effect is actually present), but also partially occludes the left subclavian artery (see details reported in the box View 1 of Fig. 2).

Following the definitions proposed by [19], we have also measured two main quantities resuming the geometry of the protruded graft: (i) the protrusion extension, defined as the length of the graft protrusion not in contact with the aortic wall; (ii) the angle ϑ between the tangential direction to the inner wall of the aortic arch and the protruded segment of the graft wall. We have performed such measurements using the tools available in Osirix (www.osirix-viewer.com) and in particular exploiting the 2D multi-planar reconstruction to select the cutting plane corresponding to the maximum graft protrusion extension.

Moreover, the distal prosthesis, at the level of the lower descending aorta, is unable of opening completely the "stenosis" of the true lumen induced by the false lumen and already present in the pre-operative case (see details reported in the box View 2 of Fig. 2). In fact, assuming as a reference the lumen area of the upper thoracic aorta, prior to the intervention the "stenosis" is around 87 % while after the graft apposition is equal of 65 %; this means that the intervention contributes to the enlargement of the true lumen but the "stenosis" remains significant, i.e., ≥ 50 %.

2.3 The CFD cases

Our study is directed to assess global hemodynamics conditions of the overall aorta, as well as of three specific aortic regions, namely: (i) the inner part of the aortic arch, where the bird-beak drawback is evident; (ii) the partially covered entry of the left subclavian; and (iii) the distal part of the thoracic aorta characterized by a significant lumen narrowing.

We have also exploited the capability of computer-based simulations to explore *what-if scenarios*; thus, our study is based on three different CFD analyses, each of them based on a specific aortic lumen configuration:

- case A: pre-operative lumen;
- case B: as-is post-operative lumen;

– case C: post-operative lumen without "stenosis" of the distal thoracic aorta.

The latter case, i.e., virtual no-stenosis case, is obtained fictitiously enlarging the distal "stenosis" in order to create a smooth tapered profile of the thoracic aorta. We perform such a modification keeping the original centerline of the stenotic vessel tract and using it as a rail for the sweeping of circular sections, having a variable diameter accomplishing the vessel tapering. This modification aimed at investigating a virtual scenario where lumen narrowing would be mitigated or resolved during the endosurgery.

As we have pointed out in the introduction, we pursue two main goals, (a) a comparison between the pre- and post-operative configurations (cases A and B), and (b) a comparison between the real and the virtual non-stenotic post-operative (cases B and C). In pursuing (a), our main concern is on the flow in the aortic arch and the effects of the bird-beak. For this reason, in case A we do not include the descending aorta tract. As a matter of fact, the latter features the presence of the false lumen and of one entry tear. This is by far complicating the simulation in this part, which is however out of our region of interest.

On the contrary, in comparing case B and C we are concerned with the analysis of the impact of the distal "stenosis", so we keep the descending tract in the region of interest.

2.4 Mesh generation, numerical model, and simulation process

Numerical simulations have been carried out by solving the incompressible unsteady Navier-Stokes equations in the region of interest, hereafter denoted by Ω. We have assumed a Newton rheology - i.e., we assume a constant viscosity - which is commonly considered correct for large and medium size vessels [10]. Let $\boldsymbol{u}(x, y, z, t)$ and $p(x, y, z, t)$ be blood velocity and pressure, respectively, ρ the constant blood density and μ the viscosity. Then the Navier-Stokes equations read

$$\begin{aligned} &\rho\frac{\partial \boldsymbol{u}}{\partial t} + \rho(\boldsymbol{u}\cdot\nabla)\boldsymbol{u} - \nabla\cdot(\mu(\nabla\boldsymbol{u} + \nabla^T\boldsymbol{u})) + \nabla p = 0 \\ &\nabla\cdot\boldsymbol{u} = 0, \end{aligned} \tag{1}$$

for $x, y, z \in \Omega$ and $0 < t \leq T$ where T is the duration of the time interval of interest. These equations need to be completed by suitable initial and boundary conditions. The initial conditions are null velocity and pressure fields, corresponding to fluid at rest. As for the boundary conditions, we distinguish three types of boundaries. Since in this case patient-specific data are not available, we retrieve data from physical considerations (for the wall and stent struts) or from the literature (for the inflow/outflow sections), as discussed in the following.

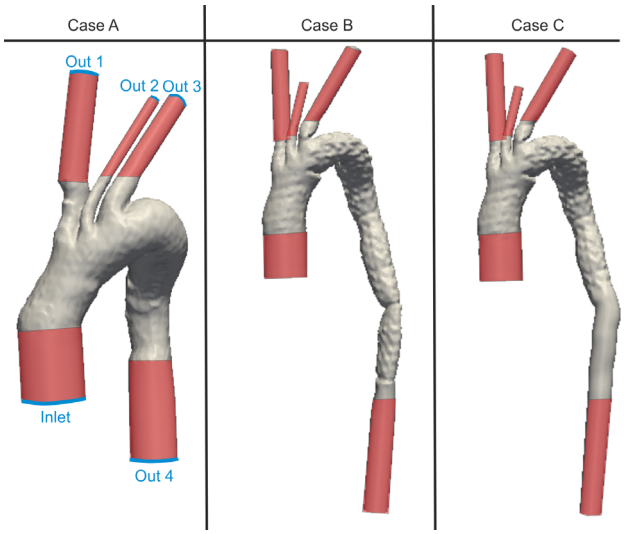

Fig. 3 Computational domains for the three investigated cases. The flow extensions are highlighted in *light red*, while the reference sections for both the inlet and outlet conditions are highlighted in *blue* and labeled as follows: *Inlet* corresponds to the inlet section of the ascending aorta; *Out 1* corresponds to the outlet section of the brachiocephalic trunk: *Out 2* corresponds to left carotid artery; *Out 3* corresponds to left subclavian; and *Out 4* corresponds to the thoracic aorta

1. We prescribe null velocity on the luminal, embedding the trace of endografts, assuming that the stented artery is rigid. Despite such an approach is commonly adopted in literature, a more accurate model would include the interaction of fluid and structure, but the computational costs would be significantly higher and the accuracy advantage questionable because the structural model for the arterial wall (differently from the blood model given by the Navier-Stokes equations) is affected by several uncertainties.
2. On the inflow section, depicted in Fig. 3, slightly distal to the aortic valve, we prescribe flow rate by selecting a velocity profile yielding at each instant the flow waveform considered in [17].
3. On the outflow sections, depicted in Fig. 3, we have prescribed conditions based on a classical three element Windkessel modeling of the distal circulation. This means that the peripheral impedance at each outflow section is represented by two resistances R_1 and R_2 and one compliance C (*RCR* model). The specific values of those parameters are taken from [14].

It is worth reminding that the region of interest Ω was artificially extended by inserting at the boundary sections cylindrical regions called *flow extensions* [17]. The role of these regions is to reduce the impact of modeling choices and uncertainties in the boundary conditions on the numerical results in the region of interest. Flow extensions have been

Table 1 Mesh details for each investigated case: (A) pre-operative; (B) as-is post-operative; (C) post-operative without distal "stenosis"

Case	Nodes	Elements	DOFs
A	258,115	1,545,810	5,669,890
B	1,219,858	6,659,921	24,859,195
C	883,994	5,375,521	19,662,539

DOFs degrees of freedom

added to Ω with the open source library *Vascular Modelling ToolKit* [1] as highlighted in Fig. 3.

It is worth noting that the same values of R_1, R_2, and C are adopted for all the cases; this assumption can be justified also for case A, where the distal part of the thoracic aorta is not included in the computational grid, under the hypothesis that the excluded vascular tract has a low impedance when compared with the imposed *RCR* boundary condition.

Numerical simulation is based on the finite element method. In this paper we use tetrahedral elements, which are particularly versatile and suited for complex geometries like the considered ones. Mesh generation is carried out using the tools available in the VMTK library. The details of the mesh for each investigated case are reported in Table 1. The problem is solved over five heart beats, arguing that the solution computed in the last heart beat reliably approximates the periodic pulsatile conditions. To perform the simulations, we use the open-source C++ library *LifeV* (www.lifev.org), developed by some of the authors in a collaborative project including EPF Lausanne, Politecnico di Milano, INRIA Paris and Emory University. As a trade-off between accuracy and computational costs, we use mixed P1bubble-P1 elements, providing piecewise continuos linear interpolation enriched by a cubic bubble for the velocity, and piecewise continuos linear approximation for the pressure.

3 Results

When analysing the numerical results, we focus our attention on certain relevant time instants of the cardiac cycle and specific regions of the aorta. More precisely, we select three time instants in the following expressed as fraction of the cardiac cycle: (i) $T1 = 0.1T$, the point of maximum acceleration of the blood flow; (ii) $T2 = 0.2T$, the systolic peak; (iii) $T3 = 0.3T$, the point of maximum deceleration of the blood flow. Following the presentation of the three cases in the previous section, we focus on the three regions of interest: (i) the inner part of the arch for cases A and B; (ii) the entry of the left subclavian artery for cases A and B; and (iii) the distal part of the thoracic artery for cases B and C.

After a brief summary of the results regarding the analysis of the post-operative lumen configuration, we report in the following the analysis of each numerical output (blood flow velocity and pressure) in each investigated case.

3.1 Analysis of the vascular geometry

For the case under investigation, the protrusion extension of the graft 1.55 cm while the angle ϑ between the tangential direction to the inner wall of the aortic arch and the protruded segment of the graft wall is almost 51°.

3.2 Velocity streamlines

Numerical simulations compute $\mathbf{u}$ and p of (1). As a matter of fact, velocity and pressure are the so-called primitive variables in the Navier-Stokes equations. For the sake of a better understanding of the results, post-processing procedure may compute secondary variables that depend on velocity and pressure. For instance the velocity streamlines, i.e., the lines whose tangents correspond at each instant and at each point with the velocity, provide an effective visualisation of blood dynamics.

3.2.1 Pre-operative (case A) versus post-operative (case B)

The pre-operative aortic arch shows a sharper angle than in the post-operative case B, leading to more pronounced disturbance in the flow.

The streamline path for this case highlights three interesting effects in the regions of interest, contoured by a red box in Fig. 4:

1. the stent-graft produces two bluffs: one at the location of the bird-beak and the second at the end of the aortic arch. Such bluffs induce boundary-layer flow separations, resulting in a disturbed flow in the arch;
2. the graft protrusion into the arterial lumen at the level of the aortic arch produces also a significant occlusion of the left subclavian artery, resulting in a backward facing step geometry of the lumen profile; this produces vortical structures in the flow, clearly not present in the other two supra-aortic branches (i.e., in the brachiocephalic trunk and in the left common carotid artery);

3.2.2 As-is post-operative (case B) versus post-operative without stenosis (case C)

The stenosis of the distal thoracic aorta due to the compression of the true lumen by the false lumen has an evident local effect on the blood flow; in fact, as highlighted by Fig. 4, a strong velocity increase and flow disturbance are present. We will see however that these effects have only a local nature, and that at the systemic level the stenosis is not introducing significant changes in the flow distribution.

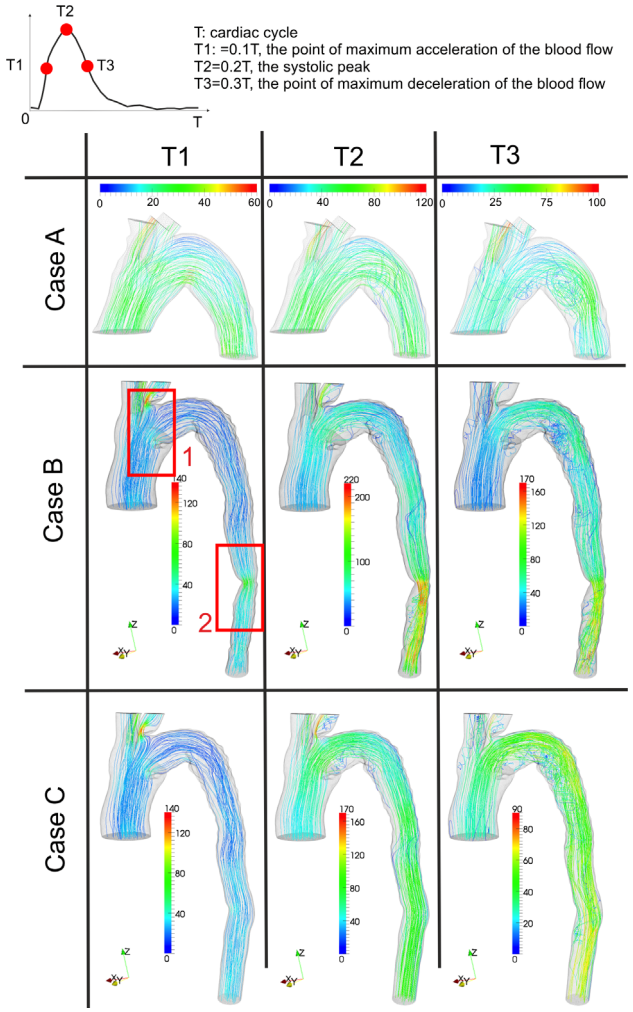

Fig. 4 Velocity streamlines for each investigated case. The corresponding velocity magnitude (cm/s) is used to color each streamline

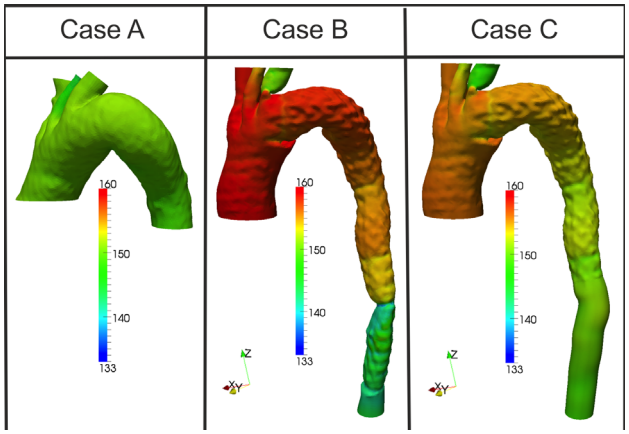

Fig. 5 Contour plot representing the distribution of blood pressure (mmHg) along the aorta in the three investigated cases at the systolic peak

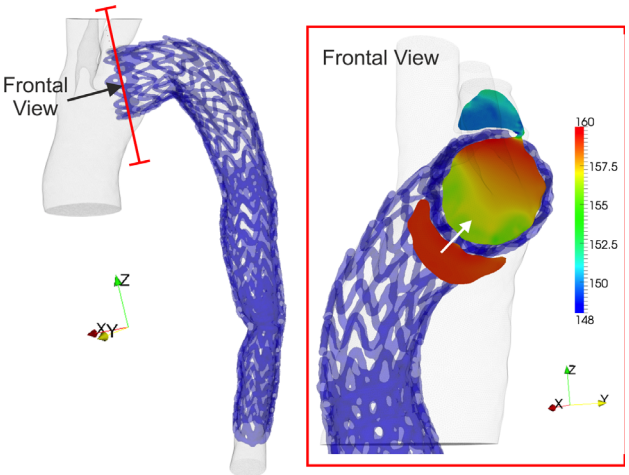

Fig. 6 Contour plot of the pressure (mmHg) distribution along a cross-section in the bird-beak region for case B

The pattern of streamlines in case C suggests that the stenosis of the distal thoracic aorta has no effect on the arch hemodynamics. At the same time, it is evident that the recovery of a smooth, physiological lumen profile eliminates the flow disturbance in this region highlighted by the results of case B.

3.3 Pressure

Figure 5 depicts the pressure distribution along the aorta at the systolic peak for the three investigated cases. For both post-operative configurations, i.e., case B and case C, it is possible to notice that the implant induces a significant pressure drop, i.e., almost 10 mmHg, at the entry of left subclavian, due to the graft protrusion which is partially occluding the branch. Indeed, the bird-beak effect and the stenosis result in a significant reduction of lumen patency and therefore in an increase of the pressure drop (by the Bernoulli's Principle, aka Venturi's effect). Instead, the pressure field is smooth in the brachiocephalic trunk, in the left common carotid artery, and in the aortic arch as in the pre-operative case. It is worth noting that in case B the stenosis induces a higher overall pressure with respect to the case with no stenosis. The global variation of pressure is in the order of 5 mmHg.

This comparison shows clearly that the removal of the lumen narrowing mitigates significantly the local pressure drop, which is in the order of 15 mmHg, as visible in the as-is post-operative configuration. Additionally, in Fig. 6 we report a virtual cross-sectional cut of the arch at the level of the bird-beak. The image, showing the contour plot of the pressure in this section, clearly reveals that a transmural pressure load difference (of almost 10 mmHg) exists between the undersurface and the luminal surface of the graft. This result confirms an observation reported in [19] highlighting a potential risk of graft infolding or collapse in that region.

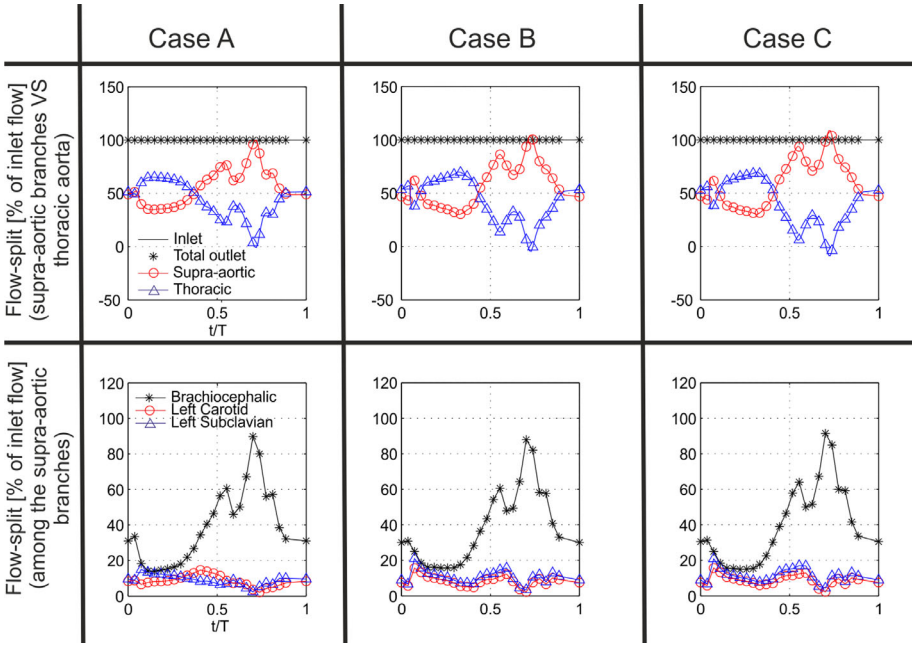

Fig. 7 Flow-split curves for each investigated cases. The top plots represent the percentage split of the inlet flow between the supra-aortic branches and the thoracic aorta. The bottom plots are instead depicting how the flow splits among each supra-aortic vessel

3.4 Flow-split

One of the concerns regarding the hemodynamic changes, induced by the endovascular implant in the aortic arch, is the potential deviation from physiologic conditions of the blood flow and the related supply to the supra-aortic branches. For this reason, we have computed the *flow-split*, i.e., how the inlet flow is divided among the outlet branches, for each investigated case. The results of such an analysis are reported in Fig. 7; they suggest that the three investigated configurations have only a minor impact on the global distribution of the inlet flows among the branches. If we focus on the flow-split between the supra-aortic vessels and the thoracic aorta, represented by the top plots in Fig. 7, we can observe that the two post-operative configurations are basically equivalent. In both cases, at the end of the diastolic phase, the flow in the thoracic aorta becomes negative (i.e., flow is directed towards the heart), while at the same time the supra-aortic branches have an over-supply of flow resulting from the sum of the inlet flow and the thoracic flow; we believe that such a phenomenon is indeed induced by the bird-beak. Nevertheless, the difference between the post-operative cases and the pre-operative one is appreciable only in early systole. These considerations are also confirmed by the values of flow-split averaged along the cardiac cycle and reported in Table 2. From this data, we can observe that the ratio of flow in the supra-aortic branches to flow in the thoracic aorta is basically 40/60, while the brachiocephalic trunk is absorbing the main part of the supra-aortic flow. This ratio is slightly different from the healthy situation, where it is assumed a ratio of 24/76 [18]. It is worth noting that the total outflow curve is perfectly superimposed to the inflow curve, indicating that the numerical solution accurately fulfils the incompressibility constraint required by the Navier-Stokes equations.

Table 2 Flow-split analysis for each investigated case: (A) pre-operative; (B) as-is post-operative; (C) post-operative without distal stenosis

Cases	A	B	C
Ascending (Inlet)	100 % (89.5)	100 % (89.5)	100 % (89.5)
Brachiocephalic	20.3 % (18.2)	20.4 % (18.3)	20.3 % (18.2)
Left carotid	9.2 % (8.2)	9.3 % (8.4)	9.4 % (8.4)
Left subclavian	11.4 % (10.2)	11.4 % (10.2)	11.4 % (10.2)
Total supra-aortic	40.9 % (36.7)	41.3 % (37.0)	41.2 % (36.8)
Thoracic	59.0 % (52.8)	58.6 % (52.5)	58.8 % (52.7)

The flow of each aortic branch over the entire cardiac cycle is reported as % of the ascending flow and also as absolute value (ml/s) between round brackets

4 Comparison of numerical results with in-vivo flow measurements

As previously mentioned, the study of hemodynamics in patient-specific cases can support the diagnostic process and medical treatment planning. However, for a reliable simulation, not only the geometrical domain, but also the considered boundary conditions (BCs) need to be patient-specific; the retrieval of patient-specific inlet and outlet BCs represents a very critical aspect. We perform a preliminary validation of our simulation predictions, comparing them with the flow measurements performed on the patient under investigation 1 year after the intervention (follow-up data). In particular, we

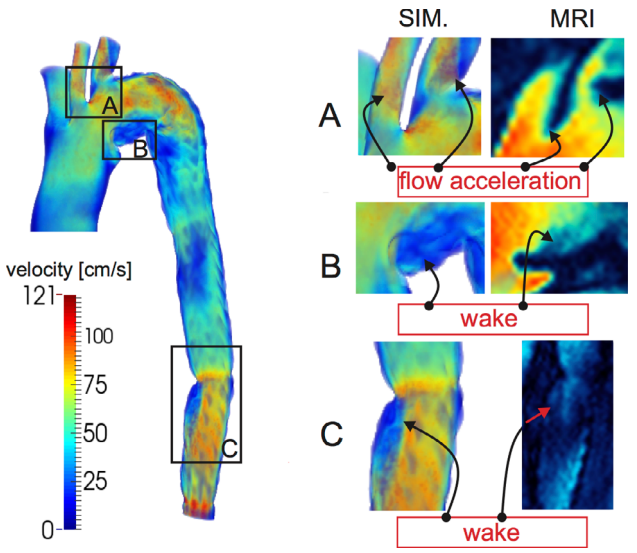

Fig. 8 Comparison with MRI data: the velocity magnitude is highlighted. On the *left*, the simulation results of the whole aorta are shown; on the *right*, the simulation results are qualitatively compared with magnetic resonance images in specific areas: **a** left carotid and subclavian arteries; **b** bird-beak zone; **c** descending aorta

perform another CFD simulation accounting for the lumen profile obtained by the follow-up MSCT, and imposing as inlet BC the flow measured by magnetic resonance through-plane PC sequences. We stress that the boundary data provide the flow rate, whilst the mathematical model would need the point-wise measurements of velocity. For this reason, these data have been called to be "defective" [10]. There are several ways to fill the gap between the available data and the mathematical requirements. Here we follow the simple strategy of prescribing an arbitrary (yet easy) velocity profile fitting the available flow rate. In this case, we select a flat velocity profile. It is worth pointing out however that this is not a patient-specific choice. The only patient-specific data included is the flow rate as described in Sect. 2.4, with the aim of comparing the obtained outflows with the data provided by the MRI. In particular, we compare the computed blood velocity and flow rate at the different aortic branches with the in-vivo measurements. In Fig. 8 a qualitative comparison between CFD analysis outcome and velocimetry measurements is presented. It is possible to observe clearly on both the left carotid artery and left subclavian artery (zoom A in Fig. 8) the Ventury's effect, and following the bird-beak (zoom B in Fig. 8) a wake with a possible flow separation. As well, a wake may be observed downstream of the "stenosis" (zoom C in Fig. 8) but that effect is less pronounced on the MRI. We notice however that the velocity represented in the MRI is a planar projection of a 3D vector, so we cannot exclude that another projection could show evident wake.

In Fig. 9 we compare the MRI and the simulation outflows. The results are not exactly matching but they are of the same

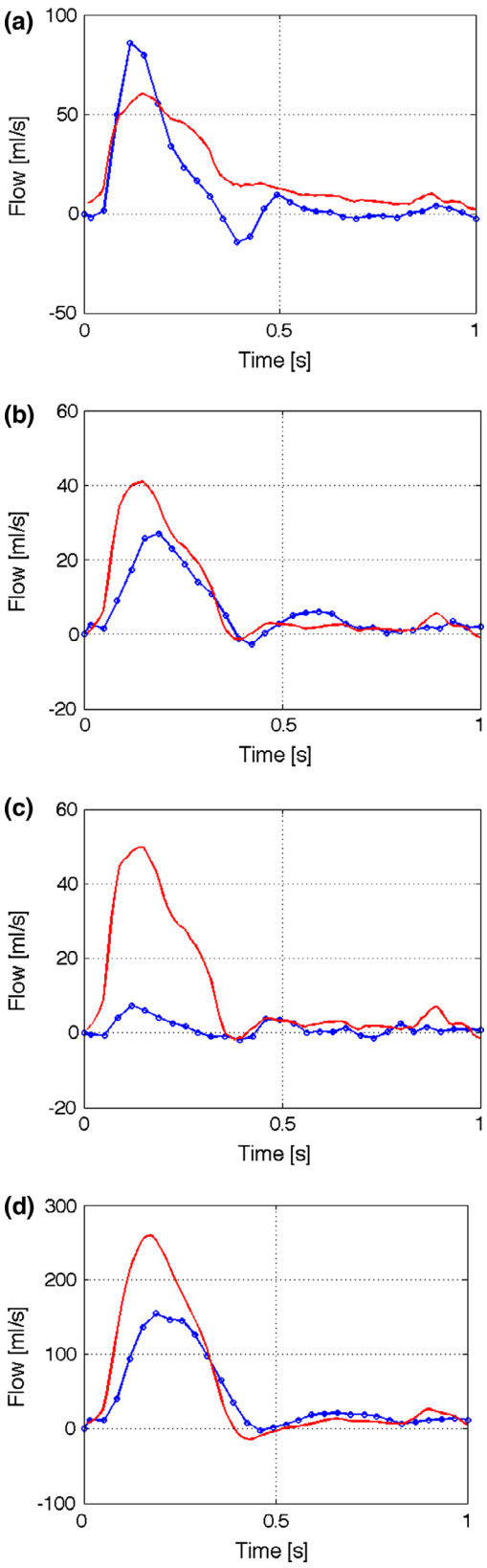

Fig. 9 Comparison of the numerical outcomes (*red solid line*) with MRI through-plane PC data (*blue soils-dotted line*). From top to bottom, flow profile in the brachiocephalic artery, left carotid artery, left subclavian artery, and descending aorta

order for the brachiocephalic trunk, the left carotid artery and the descending aorta. However, for the left subclavian carotid the flows differ significantly. As previously mentioned, the outflows are not patient-specific and the RCR values are taken from the literature. Additionally, for the particular case of the left subclavian artery a bypass has been surgically performed, which is not taken into account in the simulation.

5 Discussion

The present study addresses the quantitative analysis of the aortic hemodynamics after TEVAR. In particular, we focus on a single clinical case, basing our analysis on a patient-specific geometrical model derived from medical image analysis.

The results of our analysis suggest interesting considerations regarding this specific case. In fact, although the main clinical concern was firstly directed to the bird-beak drawback, the CFD simulations have demonstrated that there are two other important areas where the local hemodynamics is impaired and disturbed blood flow is present: the first one is the ostium of the subclavian artery, which is partially closed by the graft; the second one is the stenosis of the distal thoracic aorta.

The peculiarity of the case under investigation induced us also to compute the hemodynamic conditions for both the pre-operative configuration and a *virtual* post-operative configuration in which the lumen narrowing located in the distal part of the thoracic aorta, not removed by the graft implant, was fictitiously mitigated to resemble a smooth, more physiologic configuration. The computed pre-operative hemodynamics of the aortic arch when compared with the post-operative condition suggests that the bird-beak actually decreased the flow disturbance, which was present due to the particular pre-operative shape of the aorta of the patient. Due to the distinctive features of the pre-operative geometry, this result cannot be generalized, and we expect that in a general case the presence of the bird-beak actually increases the disturbance of the flow. In any case, as expected, the removal of the distal stenosis reduces significantly both the flow disturbance and the pressure drop across the considered arterial tract.

Besides the clinical relevance of these specific findings, the added value of these simulations is clear; in fact, CFD analyses allow to observe important flow effects that result from the specificities of patient vessel geometries.

Consequently, our results are reinforcing the potential impact of the translation of knowledge from computational biomechanics to clinical practice and viceversa. It is important to note that this process is steadily evolving; in fact our results follow the path described by other few numerical studies regarding post-TEVAR hemodynamics, which are already available in the literature. Lam et al. [15] in 2008 computed through CFD the displacement force acting on a stent graft; using the information obtained from CT-imaging, they tailored an ideal model of both the aorta and the implanted stent graft to a patient-specific geometrical features (adjusting geometrical features such as luminal diameter), in order to investigate the impact of the stent graft apposition on the displacement force acting on the stent graft. The same approach has been also pursued by [4,11].

Figueroa et al. [8] in 2009 assessed the displacement forces acting on thoracic endografts using CFD, proving that computational methods can enhance the understanding of the magnitude and orientation of the loads experienced in vivo by thoracic aortic endografts. In a similar manner, in 2011 Prasad et al. [9,20] evaluated through computer-based simulations the biomechanical and hemodynamic forces acting on the intermodular junctions of a multi-component thoracic endograft focusing on the development of type III endoleak[5] due to disconnection of stent-graft segments. Moving from medical image analysis and using CFD combined with computational solid mechanics techniques, they predicted critical zone of intermodular stress concentration and frictional instability which effectively matched the location of the type III endoleak observed during follow-up CT-imaging after 4 years.

Midulla et al. [16] in 2012 reported the use of MR angiography, followed by cardiac-gated cine sequences, covering the whole thoracic aorta, to obtain CFD boundary conditions, and tracking also the aortic wall movements. They evaluated twenty patients characterized by different aortic lesions showing the feasibility and potential of dedicated CFD analysis to provide detailed functional analysis of thoracic aorta after stent-graft implantation.

Even more recently, Pasta et al. [19] described a computational study aimed at assessing the biomechanical implications of excessive post-operative graft protrusion into the aortic arch by simulating the structural load and quantifying the fluid dynamics on the graft wall protrusion. Their findings suggest that protrusion extension leads an apparent risk of distal end-organ malperfusion and proximal hypertension, being also proportional to a pressure load acting across the graft wall, potentially portending graft collapse; these results are confirmed by our findings.

6 Limitations

Although the present study tackles a real clinical problem and based on the analysis of patient-specific data, the investiga-

[5] Type III endoleaks can occur when there is a defect in the fabric of the graft, due to tear induced by the stent fracture, or due to separation of the modular components of the endograft.

tion of a unique case limits the extension of our medical conclusions to a more general scenario. However, it is worth noting that the case under investigation is so complex and peculiar that it is difficult to collect a large population of similar situations; in addition, the data necessary to perform the presented analyses are not easy to collect, and it is not straightforward to assembly the necessary interdisciplinary knowledge, calling for a deeper and conscious collaboration between clinicians and biomedical engineers/researchers. Nevertheless, the present study poses indeed the basis for further studies involving a larger clinical dataset.

Another relevant aspect to be further investigated is the validation of the proposed results and the use of patient-specific BCs. Towards this direction, we have proposed a preliminary comparison calling for a deeper and quantitative assessment of the relation between the simulation prediction and the in-vivo measurements. Hopefully, such a limitation will be addressed and removed in future works.

Finally, in this study the presence of the endografts within the aorta is included indirectly through the description of their trace in the 3D lumen profile, resulting from image segmentation. Such an approach can be certainly improved to provide a better resolution of the impact of the graft strut protrusion in the blood flow, as proven by recent studies addressing the numerical analysis of post-stenting haemodynamics of cerebral aneurysm [22,23] or of arterial bifurcations [5,7].

7 Conclusions

With this study we propose comprehensive investigation of the aortic hemodynamics for a specific, complex clinical case through patient-specific computational fluid dynamics. The impact of the endovascular prosthesis implant, and in particular of its peculiar configuration called *bird-beak* effect, has been investigated. The numerical results suggest that the implant induces a blood flow disturbance at the level of the bird-beak but also in two other vascular regions, which were not identified by the sole clinical analysis. Besides the clinical relevance of these specific findings, this study clearly demonstrates how CFD analyses allow to observe important flow effects resulting from the specificities of patient vessel geometries. Consequently, our results are reinforcing the potential impact of the translation of knowledge from computational biomechanics to clinical practice and viceversa.

Acknowledgments This work is partially funded by: the Cariplo Foundation through the Project no. 2009.2822; ERC Starting Grant through the Project ISOBIO: Isogeometric Methods for Biomechanics (No. 259229); Ministero dell'Istruzione, dell'Università e della Ricerca through the Project no. 2010BFXRHS. The authors would like to acknowledge: Dr. T. Passerini for the support regarding the computational analysis; MD Matteo Pegorer, MD Jip Tolenaar, and MD G. H. W. van Bogerijen for the support regarding the data collection and clinical considerations; S. Marconi and Dr. M. Piccinelli for the support regarding the medical image elaboration. Moreover, Regione Lombardia and CINECA Consortium through a LISA Initiative (Laboratory for Interdisciplinary Advanced Simulation) 2013 grant are gratefully acknowledged.

Conflict of interest The authors have no commercial, proprietary, or financial interest in any products or companies described in this paper.

References

1. Antiga L (2012) VMTK:Vascular Modeling Toolkit. Accessed 1 May 2013. http://www.vmtk.com
2. Auricchio F, Conti M, Marconi S, Reali A, Tolenaar JL, Trimarchi S (2013) Patient-specific aortic endografting simulation: from diagnosis to prediction. Comput Biol Med 43(4):386–394. doi:10.1016/j.compbiomed.2013.01.006. URL http://www.sciencedirect.com/science/article/pii/S0010482513000206
3. Canaud L, Alric P, Desgranges P, Marzelle J, Marty-Ané C, Becquemin JP (2010) Factors favoring stent-graft collapse after thoracic endovascular aortic repair. J Thorac Cardiovasc Surg 139(5):1153–1157
4. Cheng SW, Lam ES, Fung GS, Ho P, Ting AC, Chow KW (2008) A computational fluid dynamic study of stent graft remodeling after endovascular repair of thoracic aortic dissections. J Vasc Surg 48(2):303–310
5. Chiastra C, Morlacchi S, Pereira S, Dubini G, Migliavacca F (2012) Computational fluid dynamics of stented coronary bifurcations studied with a hybrid discretization method. Eur J Mech - B/Fluids 35:76–84
6. Czerny M, Funovics M, Sodeck G, Dumfarth J, Schoder M, Juraszek A (2010) Long-term results of thoracic endovascular aortic repair in atherosclerotic aneurysms involving the descending aorta. J Thorac Cardiovasc Surg 140:84–S179. doi:10.1016/j.jtcvs.2010.06.031
7. De Santis G, Trachet B, Conti M, De Beule M, Morbiducci U, Mortier P, Segers P, Verdonck P, Verhegghe B (2013) A computational study of the hemodynamic impact of open- versus closed-cell stent design in carotid artery stenting. Artif Organs 37(7):E96–E106
8. Figueroa C, Taylor C, Chiou A, Yeh V, Zarins C (2009) Magnitude and direction of pulsatile displacement forces acting on thoracic aortic endografts. J Endovasc Ther 16(3):350–358
9. Figueroa CA, Zarins CK (2011) Computational analysis of displacement forces acting on endografts used to treat aortic aneurysms. In: McGloughlin T (ed) Biomechanics and mechanobiology of aneurysms, studies in mechanobiology, tissue engineering and biomaterials, vol 7. Springer, Berlin Heidelberg, pp 221–246
10. Formaggia L, Quarteroni A, Veneziani A (eds) (2009) Cardiovascular Mathematics. MMS. Springer, Milan
11. Fung GS, Lam S, Cheng SW, Chow K (2008) On stent-graft models in thoracic aortic endovascular repair: a computational investigation of the hemodynamic factors. Comput Biol Med 38(4):484–489
12. Jonker F, Schlosser F, Geirsson A, Sumpio B, Moll F, Muhs B (2010) Endograft collapse after thoracic endovascular aortic repair. J Endovasc Ther 17(6):725–734
13. Kasirajan K, Dake MD, Lumsden A, Bavaria J, Makaroun MS (2012) Incidence and outcomes after infolding or collapse of thoracic stent grafts. J Vasc Surg 55(3):652–658
14. Kim H, Vignon-Clementel I, Figueroa C, LaDisa J, Jansen K, Feinstein J, Taylor C (2009) On coupling a lumped parameter heart model and a three-dimensional finite element aorta model. Ann Biomed Eng 37(11):2153–2169. doi:10.1007/s10439-009-9760-8. URL http://dx.doi.org/10.1007/s10439-009-9760-8

15. Lam S, Fung G, Cheng S, Chow K (2008) A computational study on the biomechanical factors related to stent-graft models in the thoracic aorta. Med Biol Eng Comput 46:1129–1138
16. Midulla M, Moreno R, Baali A, Chau M, Negre-Salvayre A, Nicoud F, Pruvo JP, Haulon S, Rousseau H (2012) Haemodynamic imaging of thoracic stent-grafts by computational fluid dynamics (cfd): presentation of a patient-specific method combining magnetic resonance imaging and numerical simulations. Eur Radiol 22(10):2094–2102. doi:10.1007/s00330-012-2465-7. URL http://dx.doi.org/10.1007/s00330-012-2465-7
17. Morbiducci U, Ponzini R, Rizzo G, Cadioli M, Esposito A, Cobelli F, Maschio A, Montevecchi F, Redaelli A (2009) In vivo quantification of helical blood flow in human aorta by time-resolved three-dimensional cine phase contrast magnetic resonance imaging. Ann Biomed Eng 37(3):516–531. doi:10.1007/s10439-008-9609-6. URL http://dx.doi.org/10.1007/s10439-008-9609-6
18. Nichols W, O'Rourke M, Charalambos V (2005) McDonald's blood flow in arteries: theoretical, experimental and clinical principles. Hodder Education Publishers, Abington
19. Pasta S, Cho JS, Dur O, Pekkan K, Vorp DA (2013) Computer modeling for the prediction of thoracic aortic stent graft collapse. J Vasc Surg 57(5):1353–1361. doi:10.1016/j.jvs.2012.09.063. URL http://www.sciencedirect.com/science/article/pii/S074152141202099X
20. Prasad A, To L, Gorrepati M, Zarins C, Figueroa C (2011) Computational analysis of stresses acting on intermodular junctions in thoracic aortic endografts. J Endovasc Ther 18(4):559–568
21. Shukla AJ, Jeyabalan G, Cho JS (2011) Late collapse of a thoracic endoprosthesis. J Vasc Surg 53(3):798–801
22. Takizawa K, Schjodt K, Puntel A, Kostov N, Tezduyar T (2012) Patient-specific computer modeling of blood flow in cerebral arteries with aneurysm and stent. Comput Mech 50(6):675–686
23. Takizawa K, Schjodt K, Puntel A, Kostov N, Tezduyar T (2013) Patient-specific computational analysis of the influence of a stent on the unsteady flow in cerebral aneurysms. Comput Mech 51(6):1061–1073
24. Ueda T, Fleischmann D, Dake MD, Rubin GD, Sze DY (2010) Incomplete endograft apposition to the aortic arch: bird-beak configuration increases risk of endoleak formation after thoracic endovascular aortic repair. Radiology 255(2):645–652
25. Yushkevich P, Piven J, Hazlett H, Smith R, Ho S, Gee J, Gerig G (2006) User-guided 3D active contour segmentation of anatomical structures: significantly improved efficiency and reliability. NeuroImage 31:1116–1128